Applied and Computational Mechanics 9 (2015) 103–126

Crack path modelling in railway wheel under rolling contact fatigue

M. Kotoul[a,*]

[a] *Brno University of Technology, Faculty of Mechanical Engineering, Technická 2, 616 69, Brno, Czech Republic*

Received 22 October 2015; received in revised form 23 November 2015

Abstract

A computational model of crack path for two-dimensional primary crack situated in a railway wheel rim is designed. The railway wheel rim is placed on the wheel disc of railway wheel with interference fit. Crack behaviour is analysed in the case of rectilinear ride of a train under rolling contact fatigue. Plank and Kuhn criterion is used to decide whether crack will either kink and follow mode I controlled (tensile mode) path, or it will propagate coplanar mode II controlled (shear mode). If mode I controlled crack growth is more probable then a direction of crack propagation is predicted using the maximum tensile stress range criterion. In this way a relationship between stress intensity factors and crack geometry is obtained. For comparison, crack behaviour in a solid railway wheel which is not subjected to pre-stress loading is also analysed. In the latter case the contact forces in the wheel-rail contact are considered to have i) only normal part ii) both the normal part and tangential part.
© 2015 University of West Bohemia. All rights reserved.

Keywords: rolling contact fatigue crack, non-proportional loading, mixed mode, railway wheel, FEM

1. Introduction

It is a matter of fact that fatigue crack growth in railway wheels may lead to the loss of a part of the wheel (spalling) or to radial crack extension. The result can be damage of rails and sleepers or vehicle wheel (spalling) or a radial crack extension. The result can be damage of rails and sleepers or vehicle components or even derailment. Obviously, with increasing train speed and axle load, the rolling contact fatigue will grow in importance. There is a great number of papers devoted to the problem of wheel-rail interaction. A reader is referred to the overviews [2, 5, 10, 11, 14, 20, 28, 31, 32, 34, 36].

Fatigue cracks tend to initiate at the wheel tread [10] near the contact between wheel and rail where plastic deformation develops. Due to ratcheting of surface material fatigue cracks are initiated. Such an initiation is promoted by the occurrence of material defects. It was observed [12] that ratcheting-induced surface cracks initially propagate at a shallow angle which soon deviates into almost radial direction. Depending upon the applied loading, the crack can later deviate into a circumferential direction. Another mechanism of crack initiation at the wheel thread is connected with formation of wheel flats when the wheel slides on the rail. After extreme thermal loading due to friction between rail and wheel, rapid cooling takes place when the wheel is released and the heat is conducted into surrounding cold wheel area. As a consequence, high surface tensile stresses develop and may cause crack initiation at microscopic notches. Moreover, a brittle zone of martensite may form and, consequently, cracks are initiated. They can further propagate as fatigue cracks.

*Corresponding author. Tel.: kotoul@fme.vutbr.cz, e-mail: +420 604 229 523.

Nomenclature

a	crack depth	$\Delta K_I = K_{I\max} - K_{I\min}$,	stress intensity factor
b	lateral dimension of contact patch	$\Delta K_{II} = K_{II\max} - K_{II\min}$	ranges for modes I and II
c	width of contact patch	$\Delta K_I^*, \Delta K_{II}^*$	cyclic stress intensity range at the short supplementary crack kink under non-proportional mixed mode loading
p	contact pressure		
$v_{rel,x}$	relative velocity at the contact patch		
x_L, y_L	local coordinate system		
x_G, y_G	global coordinate system	$\overline{K_{II}}$	mean value of K_{II} during the mode I cycle
A_{ij}^{IJ}, B_{ij}^{IJ}	influence matrices		
E	Young's modulus	ΔK_{IIeff}	effective mode II range
G	shear modulus	K_{eq}	equivalent stress intensity factor
ν	Poisson's ratio	ΔK_{th}	threshold of fatigue crack growth for the cyclic mode I
N_c	normal force		
R	wheel radius	ΔK_{IIth}	threshold of fatigue crack growth for the cyclic mode II
T	tangential force		
V	rolling velocity	N	number of cycles
ΔT	time interval of the examined load cycle	$\Delta\sigma_{n,\max}$	maximum tensile stress range
		α_1, α_2	contact position angle
f	friction coefficient between the wheel and rail	α_3	contact position at the start of mode I cycle
μ	friction coefficient between crack faces	α_4	contact position at the end of mode I cycle
K_I, K_{II}	stress intensity factors for modes I and II	φ	crack deviation angle
		$\Delta\varphi$	range of crack deviation angle

The rolling contact fatigue is characterized by non-proportional mixed loading. Both shear stress controlled and normal stress controlled crack growth was reported. An existing pre-crack will either kink and will follow mode I controlled (tensile mode) path, or will propagate coplanar mode II controlled (shear mode) [26]. The general conclusion is drawn stating that non-proportional superposition of modes clearly affects the propagation behaviour of fatigue cracks. Both the crack growth rate and the direction of propagation are influenced by this. Maximum growth rate criterion proposed by Hourlier and Pineau [16] can be used to decide between tensile mode and co-planar shear mode crack growth. According to the experimental data, see e.g. [15,37], a phase shift from proportional loading to non-proportional loading leads to an increase in fatigue life if the test is performed in a stress or load controlled condition. This increase may be explained by a smaller local cyclic plastic deformation when load maxima do not coincide.

Crack propagation rates in tensile mode often appear to be significantly lesser than the coplanar growth rates. Plank and Kuhn [26] suggested that for initiating coplanar crack growth the effective mode II range (i.e. the mode II range reduced due to a possible crack surface friction) must exceed a material-specific threshold value

$$\Delta K_{IIeff} > \Delta K_{IIth} \tag{1}$$

and, additionally

$$|\Delta K_{II}| > \Delta K_I^* \left(\Delta\varphi\right), \tag{2}$$

where ΔK_{II} denotes the mode II range on the starter crack and $\Delta K_I^*(\Delta\varphi)$ stands for the range of stress intensity on the infinitesimally short supplementary crack and $\Delta\varphi$ is the range of crack deviation angle φ. The range $\Delta\varphi$ is calculated from supplementary crack positions satisfying

the local symmetry criterion $\Delta K_{II}^{*} = 0$. Namely, $\Delta\varphi = \varphi_{\max} - \varphi_{\min}$, where $\varphi_{\max}$, $\varphi_{\min}$ are two extreme angular positions for which the K_I^{*} reaches its maximum value under maximum and/or minimum load. A stress intensity range on the infinitesimally short supplementary crack is then as follows

$$\Delta K_I^{*}(\Delta\varphi) = K_{I\max}^{*}(\varphi_{\max}) - K_{I\max}^{*}(\varphi_{\min}). \tag{3}$$

As pointed out by Doquet and Pommier [9], it is questionable whether SIFs or their combinations are sufficient to describe crack growth rates under non-proportional loading because they cannot capture the complex interactions in terms of crack tip plastic flow that are likely to be loading path-dependent and to vary with the material behaviour. On the other hand, as long as the linear fracture mechanics is valid, crack growth behaviour should be explained exclusively in terms of linear elastic parameters. The aforementioned interactions could be captured by crack path criteria and a suitably modified Paris law. However, some solutions of stress intensity factor for the surface crack subjected to the simple tensile or shear stress have been found unavailable, because rolling contact fatigue (RCF) cracks experience a complex non-proportional mixed-mode loading and complicated boundary conditions [25]. Recently lot of work was devoted to modelling of rolling contact fatigue cracks in rails, see e.g. [3, 13, 29, 35]. The reason for that is quite clear and is connected with the increasing number of failures of rails contrary to decreasing number of failures of wheel and axles. More specifically, while failures of wheels and axles have been reduced by a factor of 20 over the last century, failure of rails per train kilometre have increased by a factor of more than 2 [30]. Fatigue cracks in rails initiate in the direction of wheel motion with a shallow angle of 20–30 degrees to the surface. They may branch down under repeated contact loading and propagate with a larger inclined angle to the rail surfaces, and finally lead to rail failure. For an efficient rail maintenance is it important to understand all factors that influence the fatigue propagation of short surface braking cracks. Apparently numerical tools such as FE modelling of crack growth can shed light upon this problem. Bower [7] developed a two-dimensional numerical model of surface initiated rolling contact fatigue cracks to study mode I and mode II stress intensity factors. Bogdanski et al. [2, 4, 5] have used the finite element method to examine the growth of rolling contact fatigue cracks and to predict crack tip stress intensity factors, increasing the understanding of mixed mode stress intensity factors. According to [3], the most promising models for RCF crack stress analyses are those which include liquid entrapment mechanism as it gives a considerable enhancement of the Mode I crack loading. Models developed by Kaneta et al. [23–25] included fluid pressure, which was assumed to decrease linearly along the length of the crack, being equal to the contact pressure at the crack mouth (e.g. at a railway wheel rail contact) and falling to zero at the crack tip. Stress intensity factors were calculated for circular and elliptical contact patches and semi-elliptical cracks. Most often Hertzian contact pressure distribution moving with respect to crack mouth is prescribed in FE analysis.

In this paper, we focus on FE modelling of rolling contact fatigue cracks in railway wheels. The goal is to simulate rolling contact fatigue crack growth for a two-dimensional (2D) case using FEM and taking into account a non-proportional mixed-mode loading. A parametric analysis is performed examining the influence of a friction of crack faces, presence of the tangential part of contact force and its orientation and the crack direction criterion. The analysis starts with an examination of whether a coplanar crack growth or tensile mode controlled crack growth, respectively, is more probable. It is assumed that fatigue crack growth starts, if the equivalent cyclic stress intensity ΔK_{eq} exceeds ΔK_{th}. Both, the radial crack extension and spalling are predicted and it is shown how the crack path depends on model parameters.

2. Numerical model

The starting point is the evaluation of contact forces in the wheel-rail rolling contact. The contact forces can be evaluated as an integral part of the FE analysis of rolling contact fatigue crack growth. However, such approach is extremely time- and memory-consuming one.

In order to reduce computational costs the following computational strategy consisting of two basic steps was suggested — in the first step the contact forces are evaluated using the CONTACT algorithm based on the boundary element method and developed by [21]. In the second step the FEM model is loaded with these contact forces to evaluate crack behaviour. The mentioned algorithm can be used for a contact of two bodies whose shapes cannot be replaced with a surface with a constant local curvature or for a contact of bodies which have different material properties. The algorithm treats separately the normal and tangential parts of the contact. The expected contact area is discretised and the influence matrix accordingly to the representation of Boussinesq and Cerruti [22] is calculated for each element.

By Kalker, the influence matrix of the element I in position $\boldsymbol{x_I}(x_I, y_I)$ generated by the element J is

$$\begin{aligned}
&\mathbf{A}^J(x_I, y_I) \equiv \mathbf{A}^{IJ} = \\
&= \frac{1}{\pi \cdot G} \cdot \int_{x_J-\Delta x}^{x_J+\Delta x} \int_{y_J-\Delta y}^{y_J+\Delta y} \begin{bmatrix} \frac{1-\nu}{\rho} + \frac{(x'-x_I)^3}{\rho^3} & \frac{\nu\cdot(x'-x_I)\cdot(y'-y_I)}{\rho^3} & \frac{K\cdot(x'-x_I)}{\rho^2} \\ \frac{\nu\cdot(x'-x_I)\cdot(y'-y_I)}{\rho^3} & \frac{1-\nu}{\rho} + \frac{(y'-y_I)^2}{\rho^3} & \frac{K\cdot(y'-y_I)}{\rho^2} \\ -\frac{K\cdot(x'-x_I)}{\rho^2} & -\frac{K\cdot(y'-y_I)}{\rho^2} & \frac{1-\nu}{\rho} \end{bmatrix} \mathrm{d}x'\,\mathrm{d}y',
\end{aligned} \tag{4}$$

where ρ is defined as $\rho = \sqrt{(x'-x_I)^2 + (y'-y_I)^2}$ and G, ν and K are combined material properties $\frac{1}{G} = \frac{1}{2\cdot G^{(1)}} + \frac{1}{2\cdot G^{(2)}}$, $\nu = G \cdot \left(\frac{\nu^{(1)}}{2\cdot G^{(1)}} + \frac{\nu^{(1)}}{2\cdot G^{(2)}} \right)$, $K = \frac{G}{4} \cdot \left(\frac{1-2\cdot\nu^{(1)}}{G^{(1)}} + \frac{1-2\cdot\nu^{(2)}}{G^{(2)}} \right)$, where G stands for the shear modulus, ν is Poisson's ratio and the superscripts (1) or (2) refer to the wheel or rail respectively. The x-axis of the contact patch is identical with the direction of the rolling velocity.

The deformation of the influence area is considered to be very small compared to the size of the wheel or the rail. The relation between the element displacement $u_i(x_I, y_I) \equiv u_i^I$ and the load acting on the contact patch is written as

$$u_i^I = \sum_{J=1}^{N} \sum_{j=1}^{3} A_{ij}^{IJ} \cdot p_j^J, \tag{5}$$

where p_j^J is the j-component of load acting on the element J of the contact patch and the summation is performed over all elements of the contact patch.

The normal contact pressures are found from the solution of the system of equations

$$\begin{aligned}
&e^I = h^I + u_3^I = h^I + \sum_{J=1}^{N} \sum_{j=1}^{3} A_{3j}^{IJ} \cdot p_j^J, \\
&e^I = 0 \text{ if the element } I \text{ lies inside the contact patch,} \\
&p_j^J = 0 \text{ if the element } I \text{ lies outside the contact patch,}
\end{aligned} \tag{6}$$

where $e^I$is the deformed distance and h^I is the undeformed distance. The normal force is calculated as

$$N_c = \sum_{I \in C} p_3^I \cdot \mathrm{d}S_I. \tag{7}$$

Tangential forces depend on the velocity of the vehicle, on relative velocities in the contact patch, on the normal forces and on the coefficient of adhesion. The tangential forces can be calculated similarly like the normal tractions. The basic presumption is to evaluate the influence matrices A_{ij}^{IJ} (current influence) and B_{ij}^{IJ}, (influence of the previous time step). Then the following system of equations is solved:

$$\begin{aligned} s_\tau^I &= c_\tau^I + \frac{\sum_{J=1}^{N}\sum_{j=1}^{3} A_{\tau j}^{IJ}\cdot p_j^J(t) - B_{\tau j}^{IJ}\cdot p_j^J(t-\mathrm{d}t)}{\mathrm{d}t}, \\ s_\tau^I &= 0 \text{ if element is in the adhesion area,} \\ s_\tau^I &= -S_I\cdot\frac{p_\tau^I}{f\cdot p_3^I} \text{ and } \sqrt{p_1^{I2}+p_2^{I2}} = f\cdot p_3^I \text{ if element is in the slip area } S_I, \end{aligned} \tag{8}$$

τ denotes the tangential direction on the contact surfaces, c_τ^I is the rigid slip of an element, and $s_\tau^I$is a virtual slip of an element. The time difference $\mathrm{d}t$ depends on the boundary element size $2\mathrm{d}x$ and rolling velocity V, $\mathrm{d}t = \frac{2\cdot\mathrm{d}x}{V}$. In the first step of the algorithm it is considered that the adhesion area correspond to the whole contact patch, hence the slip area is an empty set. Accordingly, the linear set of equations is solved in the first step:

$$0 = c_\tau^I + \frac{\sum_{J=1}^{N}\sum_{j=1}^{3} A_{\tau j}^{IJ}\cdot p_j^J(t) - B_{\tau j}^{IJ}\cdot p_j^J(t-\mathrm{d}t)}{\mathrm{d}t}, \tag{9}$$

The solution of (9) for the contact patch of elliptical shape corresponds to the numerical solution of Kalker's linear theory of rolling contact. Tangential forces are defined as:

$$T_x = \sum_I p_1^I\cdot\mathrm{d}S_I, \quad T_y = \sum_I p_2^I\cdot\mathrm{d}S_I. \tag{10}$$

The distribution of contact pressures [19] along the direction parallel to the wheel axis is shown in Fig. 1.

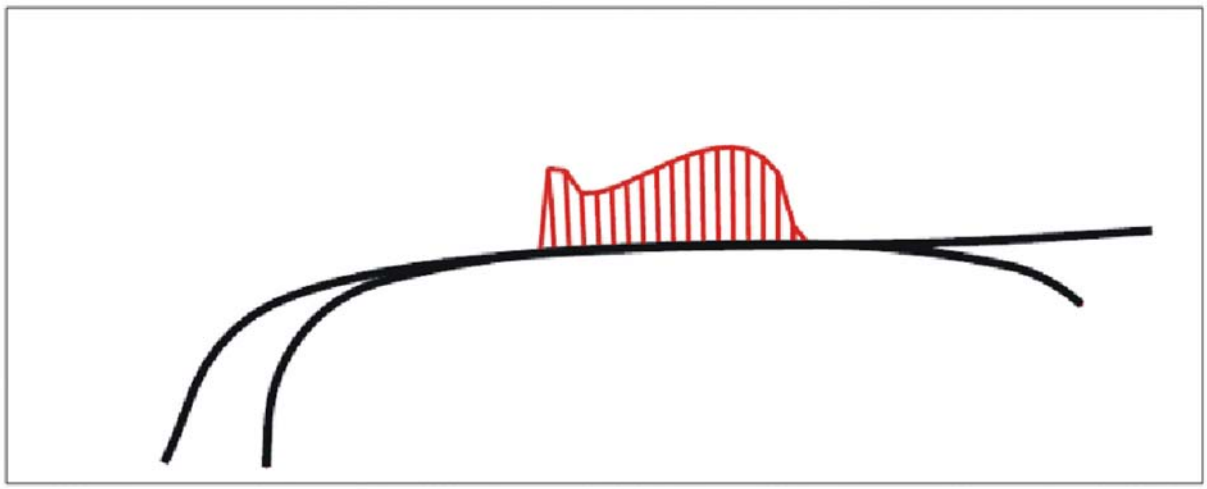

Fig. 1. Distribution of contact pressures along the direction parallel to the wheel axis

Fig. 2 shows the shape of half of the contact patch with distribution of contact pressures calculated by Hertz algorithm (upper part of figure) and by the CONTACT algorithm (lower part of figure) [19]. Apparently, the shape of the contact patch calculated using the CONTACT

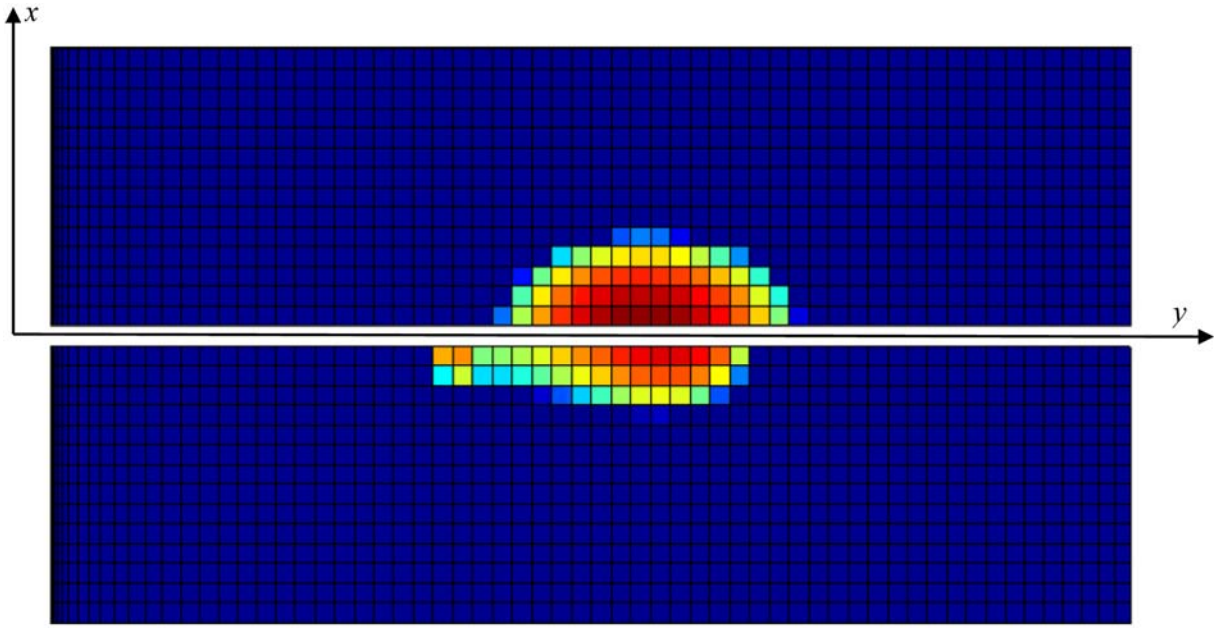

Fig. 2. Shape of half of the contact patch with distribution of contact pressures calculated by Hertz algorithm (upper part of figure) and by the CONTACT algorithm (lower part of figure)

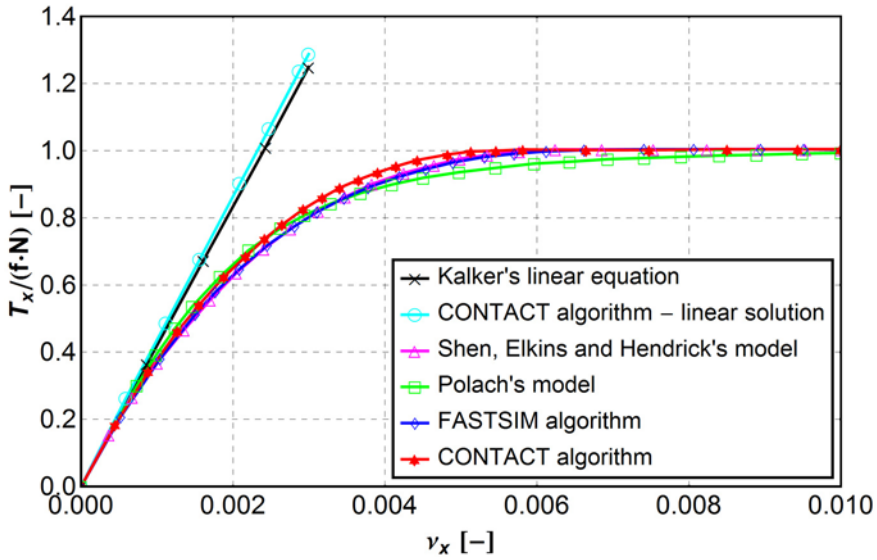

Fig. 3. Longitudinal tangential force as a function of the relative longitudinal creepage $v_x = v_{\mathrm{rel},x}/V$

algorithm differs from the Hertzian elliptic contact patch. Fig. 3 shows the longitudinal tangential force as a function of the relative longitudinal creepage $v_x = v_{rel,x}/V$ ($v_{rel,x}$ is the relative velocity at the contact patch) calculated by various methods. Except of linear solutions, the longitudinal tangential force saturates at the value fN_c.

Previous results provide a basis for transformation of 3D rolling contact to 2D rolling contact. The wheel rim is considered to be sufficiently wide so that the contact problem can be reduced to plane strain problem at least in the middle plane of the wheel. We proceed as follows — the contact area is considered to be a strip $x \in [-c, c]$ and the contact pressure is described by the

2D Hertz solution

$$p(x) = p_{\max}\sqrt{1 - \frac{x^2}{c^2}}, \quad c^2 = \frac{8N_c/b\, R(1-\nu^2)}{\pi E}, \quad p_{\max} = \frac{2N_c}{\pi c b}. \tag{11}$$

N_c/b characterizes the normal force per unit length. The value of b is taken as the lateral dimension of the contact patch (along the y-axis) calculated above, see Fig. 2 and approximately equals to 20 mm. Considering $N_c = 10^5$ N and the outer diameter of the wheel rim $2R = 920$ mm, we get a 2D Hertz contact loading prescribed within the sector of approximately $1.2°$, see Fig. 4.

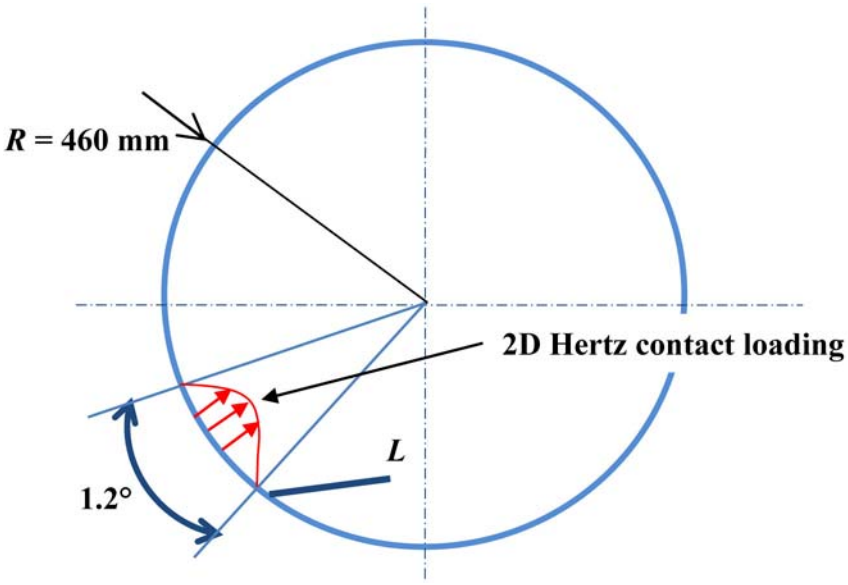

Fig. 4. 2D Hertz contact loading prescribed on the wheel rim within the sector approximately of $1.2°$

Numerical model of crack was created in the system ANSYS version 14 (ANSYS Inc., Canonsburg, PA, USA). A rectilinear ride of a train with a constant speed is assumed and no geometric imperfections of rails and/or wheel tread are considered. An initial crack of depth of 2 mm is inclined to the tangential direction with shallow angle $20°$, see Fig. 4. Such geometrical configuration is typical for railway wheels (RW) [36]. The depth of crack is increased by 0.03 mm after each loading step defined by the position of the crack mouth with respect to the contact point in the range limited by angles $\alpha_1 = -2°$ and $\alpha_2 = 5°$, see Fig. 5. As it will be shown later, outside this range both SIFs K_I and K_{II} are equal to zero if no static pre-stress is present. Note that virtually a number of cycles is required to propagate the crack of 0.03 mm. The number of cycles can be estimated for example using crack growth law developed by Bold and Brown [6]:

$$\Delta K_{eq} = \sqrt{\Delta K_I^2 + \left(\frac{614}{507}\Delta K_{II}^{3.21}\right)^{\frac{2}{3.74}}}, \tag{12}$$

$$\frac{\mathrm{d}a}{\mathrm{d}N} = 0.000\,507(\Delta K_{eq}^{3.74} - \Delta K_{th}^{3.74}),$$

where ΔK_{eq} is an equivalent stress intensity factor combining mode I and II even though the peaks of ΔK_I and ΔK_{II} are out of phase. The crack extension is performed for a wide range of deviation angle φ and the possibility of coplanar crack growth is tested using Eqs. (1) and (2).

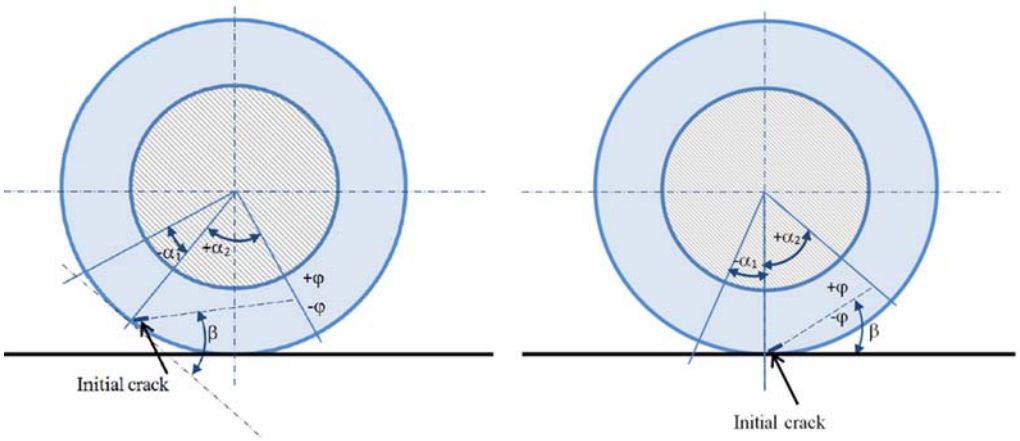

Fig. 5. Scheme of railway wheel geometry

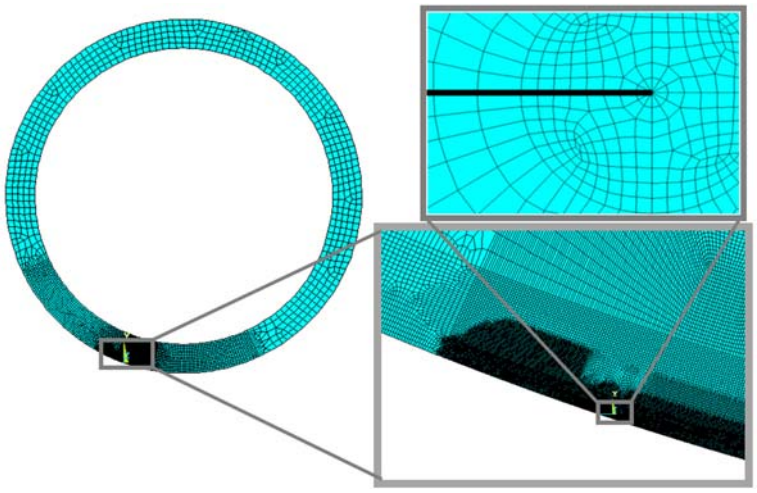

Fig. 6. FE mesh and size of discretization

Two basic configurations are considered: a crack on wheel rim fixed by an interference fit accompanied by a relative increase of the rim's inner diameter of about 1.44 % (amounting to approximately 1.11 mm), and a crack in a solid railway wheel. The outer diameter of the wheel rim is 920 mm and the thickness of the rim is 75 mm. The FE mesh consists of quadratic elements PLANE183, see Fig. 6. A sensitivity analysis of mesh has not revealed any substantial changes in the values of stress intensity factors during further mesh refinement.

The mesh was graded such that it exhibits high density near the contact and near the crack tip, see Fig. 6. It was shown elsewhere [32] that the concept of the linear elastic fracture mechanics is likely to be valid for crack modelling in rolling contact fatigue of railway wheels. Hence, a plastic zone ahead of the crack tip and related stress redistribution is not considered. The material of the wheel is assumed to be homogeneous, isotropic with the Young modulus $E = 2.1 \cdot 10^5$ MPa and Poisson's ratio $\nu = 0.3$.

The wheel is loaded by a distribution of contact pressures which correspond to the total contact force of 10 tons. The algorithm for Hertzian contact calculation was described above, for more details see e.g. [1, 17, 18]. The contact pressure data are prescribed in individual nodes of the quadratic element PLANE 183, see Fig. 7.

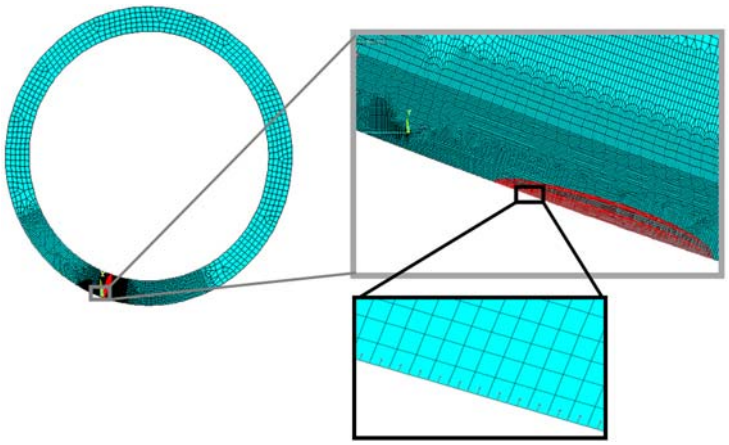

Fig. 7. Nodes of quadratic elements where the contact pressure data are prescribed

The stress intensity factors at a crack for a linear elastic fracture mechanics analysis were computed using the KCALC command in ANSYS. The analysis uses a fit of the nodal displacements in the vicinity of the crack. For full model the ANSYS software uses formulas for $\Theta = \pm 180°$ under plane strain conditions as follows:

$$K_I = \frac{1}{4}\sqrt{\frac{\pi}{2}}\frac{E}{1-\nu^2}\frac{|\Delta v|}{\sqrt{r}}, \quad K_{II} = \frac{1}{4}\sqrt{\frac{\pi}{2}}\frac{E}{1-\nu^2}\frac{|\Delta u|}{\sqrt{r}}, \quad K_{III} = \frac{1}{4}\sqrt{\frac{\pi}{2}}\frac{E}{1-\nu^2}\frac{|\Delta w|}{\sqrt{r}},$$

where u, v, w are displacements, r, Θ — coordinates in local cylindrical coordinate system, see Fig. 8 below.

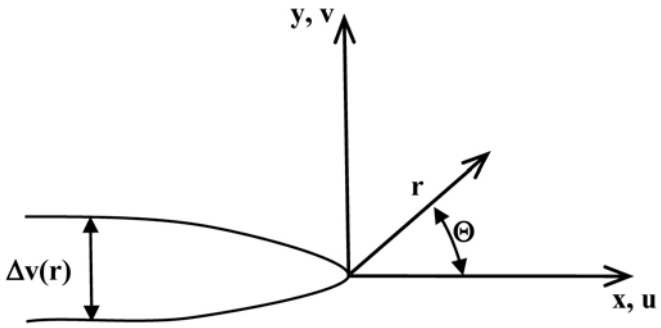

Fig. 8. Scheme of the crack and the local cylindrical coordinate system

The nodal displacements are fitted by a linear approximation like e.g. $|\Delta v|/\sqrt{r} = A + B \cdot r$. If r approaches to zero, one obtains $\lim_{r\to 0} |\Delta v|/\sqrt{r} = A$. Then equation

$$K_I = \frac{1}{4}\sqrt{\frac{\pi}{2}}\frac{E}{1-\nu^2}\frac{|\Delta v|}{\sqrt{r}}$$

will become

$$K_I = \frac{1}{4}\sqrt{\frac{\pi}{2}}\frac{E}{1-\nu^2}A.$$

Collapsing quadratic quarter-point elements and nodes were used for computing stress intensity factors at the crack tip.

3. Results and discussion

3.1. Fatigue cracks in a wheel rim

As the first, a possibility of coplanar crack growth is examined. To this purpose, the Plank and Kuhn criteria (1), (2) are tested. The K^*-factors on the short supplementary crack (0.03 mm) are calculated during one loading cycle for a different crack deviation angles aiming to look for the situation when K_I^* becomes maximum/minimum while K_{II}^* disappears. Hereafter fatigue crack growth is modelled for two cases of surface friction between the crack faces: i) without friction and ii) with friction prescribing the coefficient of friction $\mu = 0.5$. The results are shown in Fig. 9 and Fig. 10. Note that the interference fit generates a static pre-stress and, consequently, static K-factors. It is particularly seen for the mode II loading. As pointed out by Plank and Kuhn, the superposed static mode II loading may influence only the deviation and the crack propagation rate, but does not influence the crack propagation mode. Hence, ΔK_I^*, ΔK_{II}^* and also ΔK_{II} are referred to the static value which can be easily read far from the contact position with respect to crack mouth, see Fig. 9. By inspection of results in Fig. 9 one can see that the condition (2) is not fulfilled.

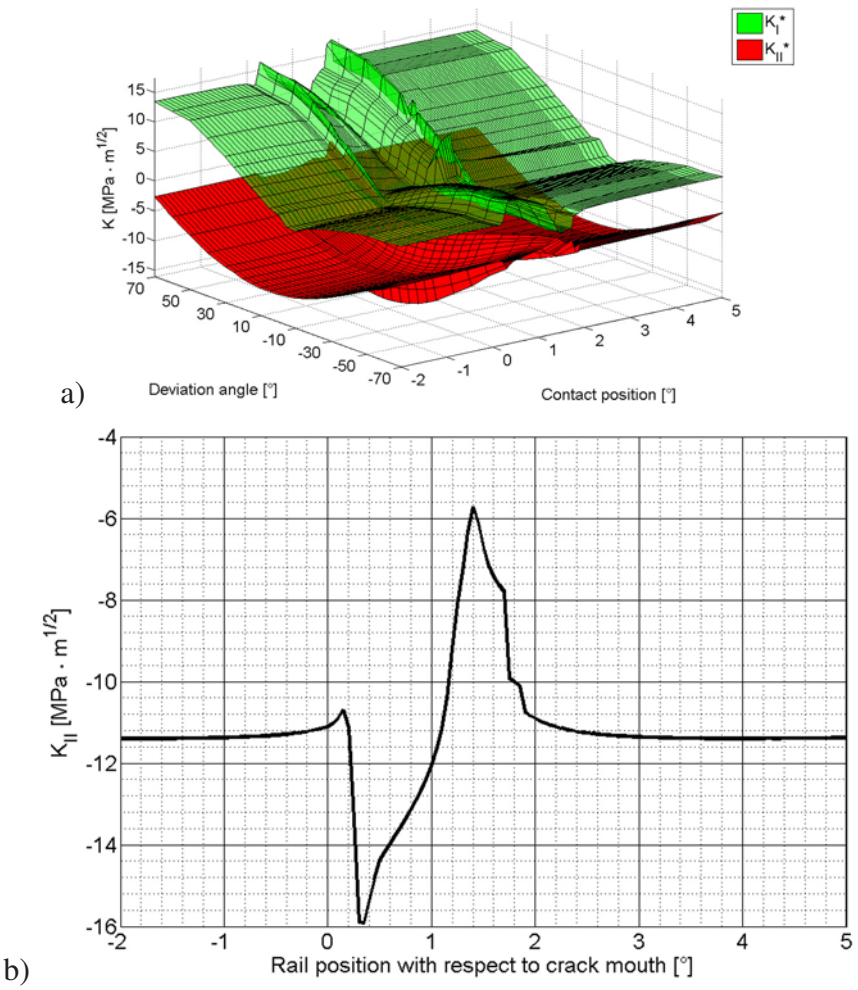

Fig. 9. a) ΔK_I^* and ΔK_{II}^* on the short supplementary crack for a wide range of crack deviation angles as functions of rolling contact position with respect to crack mouth; b) ΔK_{II} on the starter crack as a function of rolling contact position with respect to crack mouth. Friction between the crack faces is not considered

Specifically, ΔK_{II} for the starter crack takes the value of about 10 MPa m$^{1/2}$, see Fig. 9b. From Fig. 9a, it can be further deduced that $\Delta K_I^*(\Delta\varphi)$ takes also the value of about 10 MPa m$^{1/2}$ when $K^*_{I\,\max}(\varphi_{\max}) \cong 15$ MPa m$^{1/2}$ and $K^*_{I\,\max}(\varphi_{\min}) \cong 5$ MPa m$^{1/2}$ for $\varphi_{\max} \cong 70°$ and $\varphi_{\min} \cong 50°$, respectively, see also Eq. (3). The situation is even more pronounced when the surface friction between crack faces is considered, see Fig. 10. Observe in Fig. 10b that K_{II} takes the value of about -8.5 MPa m$^{1/2}$ far from the contact position with respect to crack mouth due to static pre-stress. The maximum value of K_{II} approaches zero due to superposed cyclic contact loading, hence $\Delta K_{II} \cong 8.5$ MPa m$^{1/2}$. The results shown in Fig. 10a indicate that $K^*_{I\,\max}(\varphi_{\max}) \cong 18$ MPa m$^{1/2}$ for $\varphi_{max} \cong 70°$ and $K^*_{I\,\max}(\varphi_{\min}) \cong 2$ MPa m$^{1/2}$ for $\varphi_{min} \cong -30°$, hence $\Delta K_I^*(\Delta\varphi)$ takes value of about 16 MPa m$^{1/2}$. To conclude, mode II controlled crack growth is not likely to be initiated and the crack deviates tensile mode controlled path.

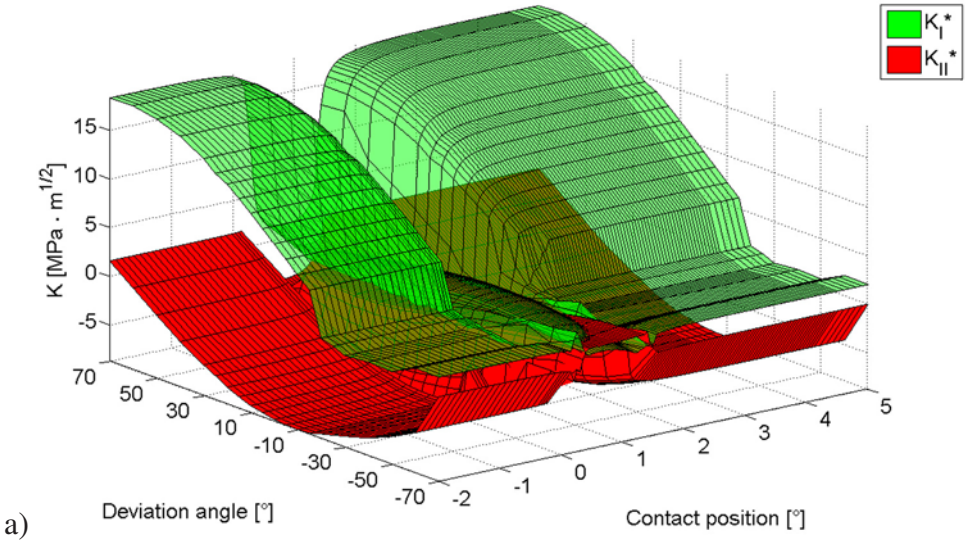

a)

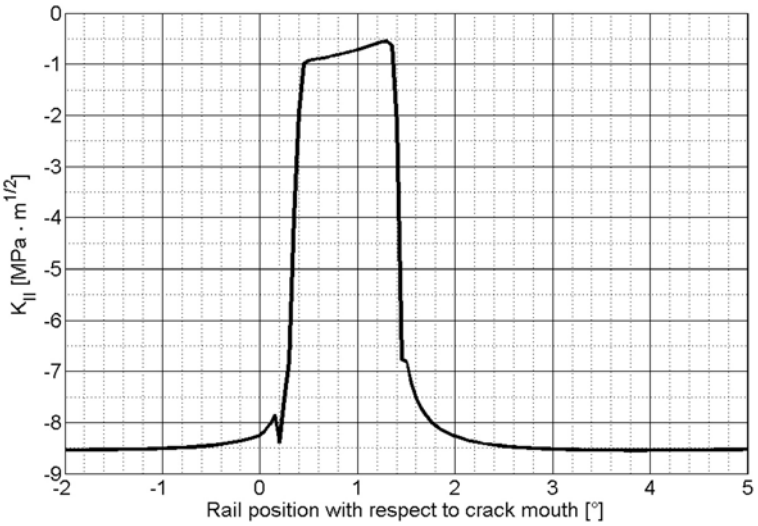

b)

Fig. 10. a) ΔK_I^* and ΔK_{II}^* on the short supplementary crack for a wide range of crack deviation angles as functions of rolling contact position with respect to crack mouth; b) ΔK_{II} on the starter crack as a function of rolling contact position with respect to crack mouth. Surface friction between the crack faces with the coefficient of friction $\mu = 0.5$

The procedure of fatigue crack path prediction under non proportional loading is based on the assumption that the crack propagates in the direction perpendicular to the direction of the maximum tensile stress range $\Delta\sigma_{n,max}$. Note that $\Delta\sigma_{n,max}$ criterion predicts well the crack path in polymodal fatigue in structural steels. The crack deviation angle, φ, is given by the maximum tensile stress range criterion as [8]

$$\Delta\sigma_{n,\max} = \max_{\varphi}\left(\max_{t\in\Delta T}(\Delta\sigma_n(\varphi,t))\right), \tag{13}$$

where t is the time, ΔT is the time interval of the examined load cycle and

$$\sigma_n(\varphi,t) = \frac{1}{4\sqrt{2\pi r}}\left[K_I(t)\left(3\cos\frac{\varphi}{2}+\cos\frac{3\varphi}{2}\right) - K_{II}(t)\left(3\sin\frac{\varphi}{2}+3\sin\frac{3\varphi}{2}\right)\right] + O(r).$$

Surprisingly, the crack deviation angle, φ, calculated from Eq. (13) differs by a few percents from the angle calculated from Richard's criterion [27]

$$\varphi = \mp\left[155.5^\circ\cdot\frac{|K_{II}|}{K_I+|K_{II}|} - 83.4^\circ\cdot\left(\frac{|K_{II}|}{K_I+|K_{II}|}\right)^2\right], \tag{14}$$

where for K_I and K_{II} their mean values during the mode I cycle are substituted. The deviation angle $\varphi<0$ for $K_{II}>0$ and $\varphi>0$ for $K_{II}<0$. The mean value of K_{II} during the mode I cycle is calculated as

$$\overline{K_{II}} = \frac{1}{\alpha_4-\alpha_3}\cdot\int_{\alpha_3}^{\alpha_4} K_{II}(x)\,\mathrm{d}x, \tag{15}$$

where α_3, α_4 correspond to contact positions when mode I cycle starts and finishes, respectively.

In the subsequent loading step the calculated kinking angle φ is used to rotate the local coordinate system x_L, y_L, see Fig. 11, and the constant crack increment of the length of 0.03 mm is then imposed.

Fig. 12 shows a predicted crack path in the global coordinate system depicted in Fig. 11, for the case when friction is not considered and for the case when the coefficient of friction between crack faces $\mu = 0.5$.

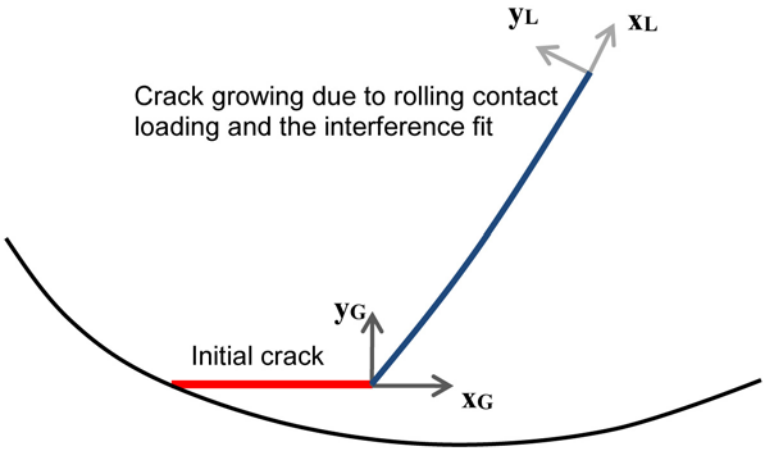

Fig. 11. Scheme of the crack configuration

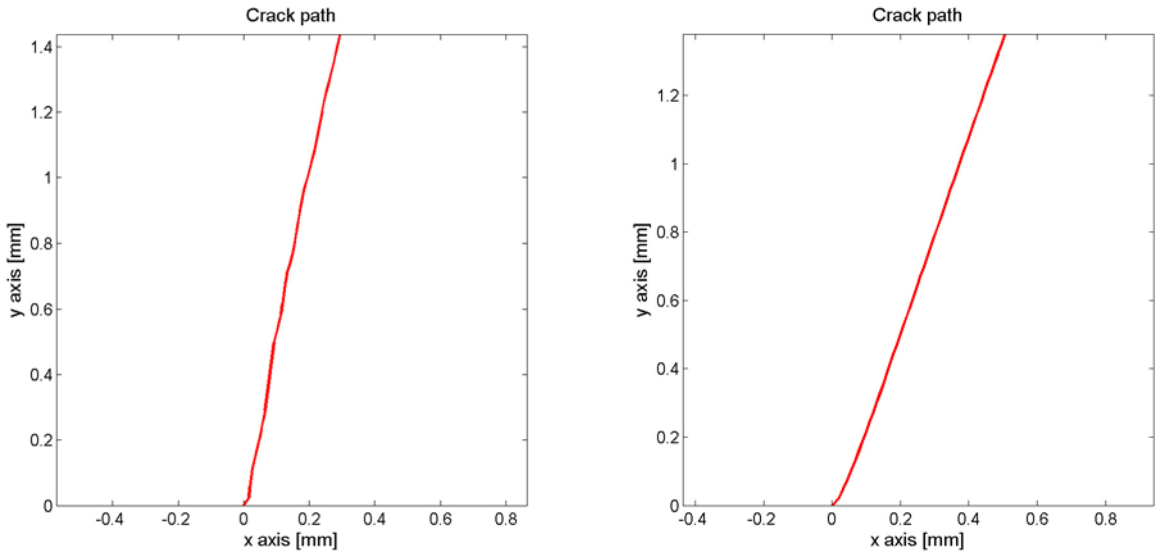

a) Without friction between crack faces b) Friction coefficient $\mu = 0.5$

Fig. 12. Predicted crack path in RW rim

Apparently, due to the interference between the rim and the wheel a radial crack extension is a preferred mode of fracture. In the case of friction between crack faces, the crack path somewhat diverts from the radial direction in comparison to the case without friction. This behaviour can be easily explained by decrease of the effective mode II stress intensity factor due to friction. As can be seen from Fig. 13, a small change of K_{II} within the range $0 \div 3K_I$ leads to a significant change of the deviation angle φ.

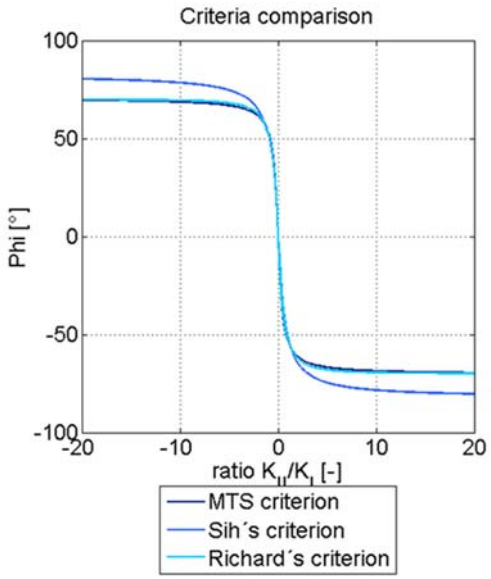

Fig. 13. Comparison of different criteria for prediction of the crack path

3D graphs in Fig. 14 show how K_I and K_{II} depend on the contact position, cf. Fig. 11, and on the crack depth. The calculations are performed for the case when the coefficient of friction between crack faces $\mu = 0.5$. Very similar results are obtained if no friction between crack faces is considered. Apparently, the amplitudes of K_I and K_{II} grow with the crack depth.

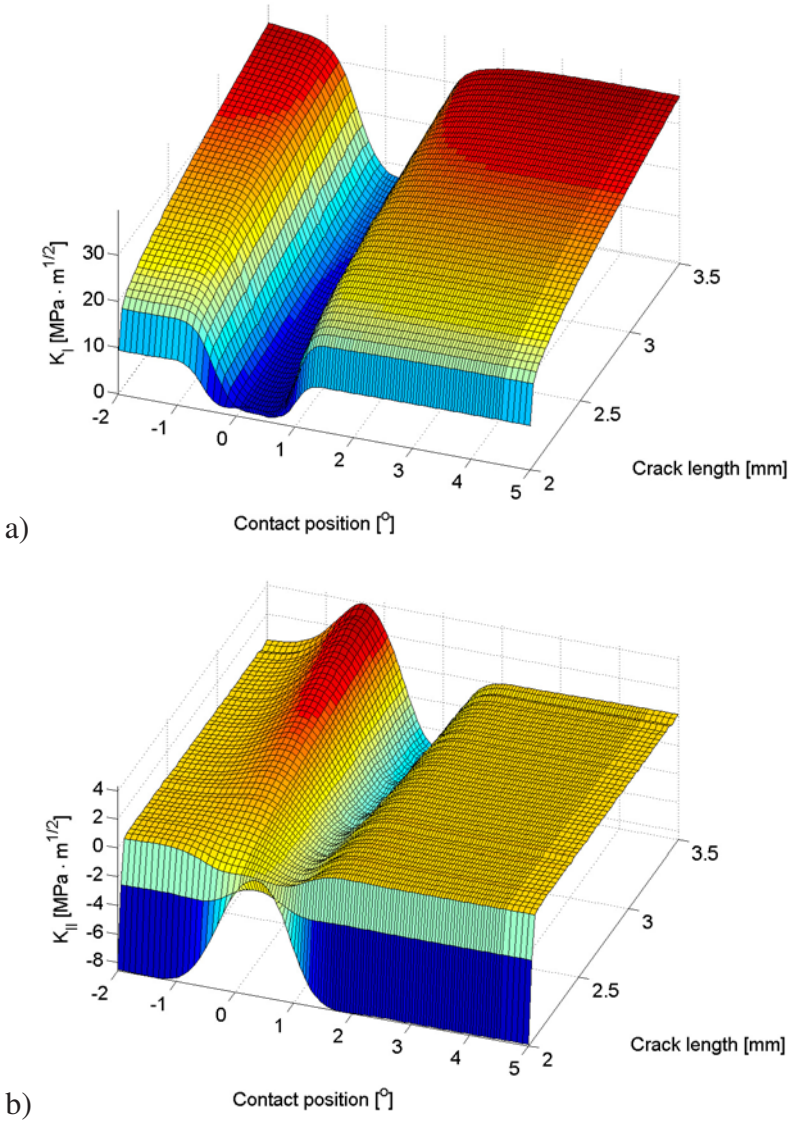

Fig. 14. K_I and K_{II} as functions of rolling contact position and crack depth

3.2. Fatigue crack path in a solid railway wheel

It is a matter of interest to compare the crack growth in the RW rim with a crack behaviour in a solid railway wheel which is not subjected to pre-stress loading.

The initial geometry of the solid railway wheel containing a crack is the same as in the case of rim wheel. Also boundary conditions and the computation algorithm are identical.

Analogously to the case of the RW rim we start examining a possibility of coplanar crack growth. Consider frictionless contact between crack faces. By inspection of the results in Fig. 15 one can see that contrary to the RW rim the condition (2) is fulfilled in the case of the solid railway wheel. Evidently, while $\Delta K_{II} \cong 9$ MPa m$^{1/2}$, $K^*_{I\max}(\varphi_{\max})$ is approximately equal to 3.5 MPa m$^{1/2}$ for $\varphi_{max} \cong 70°$ and $K^*_{I\max}(\varphi_{\min}) \cong 2$ MPa m$^{1/2}$ for $\varphi_{min} \cong -50°$, hence $\Delta K^*_I(\Delta\varphi) \cong 1.5$ MPa m$^{1/2}$. However, this is only a necessary condition, in addition, the effective mode II range must exceed a material-specific threshold value for initiating coplanar crack growth, see the condition (1). Note that a very similar result is obtained if the friction between crack faces is included.

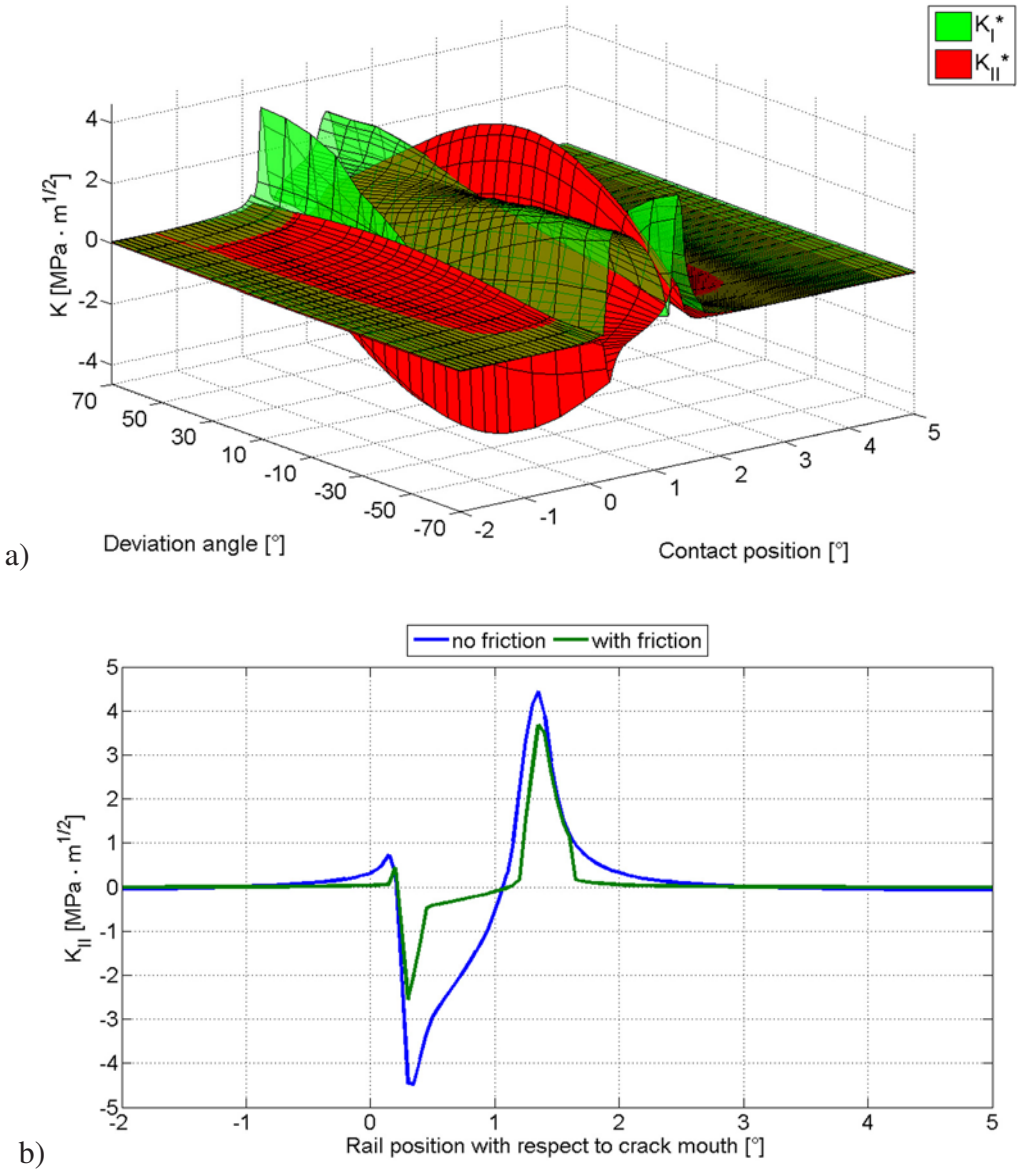

Fig. 15. a) ΔK_I* and $\Delta K*_{II}$ on the short supplementary crack for a wide range of crack deviation angles as functions of rolling contact position with respect to crack mouth; b) ΔK_{II} on the starter crack as a function of rolling contact position with respect to crack mouth

If mode II controlled crack growth is not likely to be initiated because the condition (1) is not fulfilled, the crack deviates tensile mode controlled path. Using the same methodology as in the case of RW rim, the crack path was predicted. Fig. 16a shows predicted crack path in the solid railway wheel for the case when friction is not considered while Fig. 16b pertains to the case when the coefficient of friction between crack faces $\mu = 0.1$. Apparently, crack path simulations in a solid railway wheel show that while without friction the crack follows a radial path shown in Fig. 16a, spalling is preferred mode of fracture if friction of crack faces is considered.

3D graphs in Fig. 17a, and Fig. 17b, which display the way how K_I and K_{II} depend on the contact position and on the crack depth, provide an explanation of such behaviour. Namely, while K_I changes only slightly with increasing friction between crack faces, cf. Fig. 17a and Fig. 17b, the range of K_{II} is reduced due to the crack surface friction, cf. Fig. 15b, Fig. 18a and Fig. 18b.

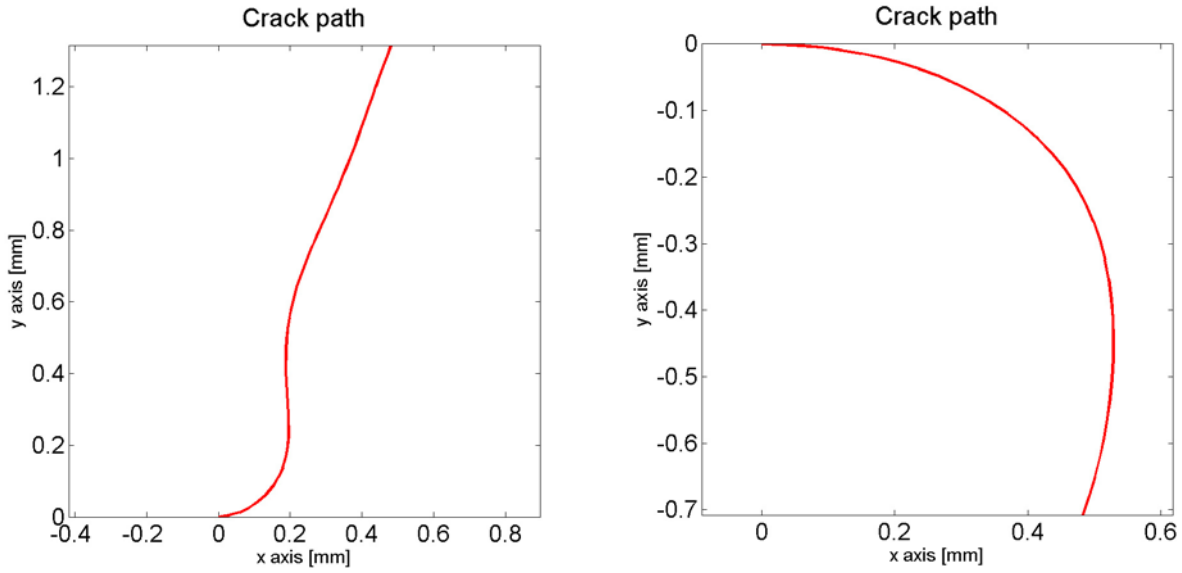

a) Without friction between crack faces b) Friction coefficient $\mu = 0.1$

Fig. 16. Predicted crack path in solid railway wheel

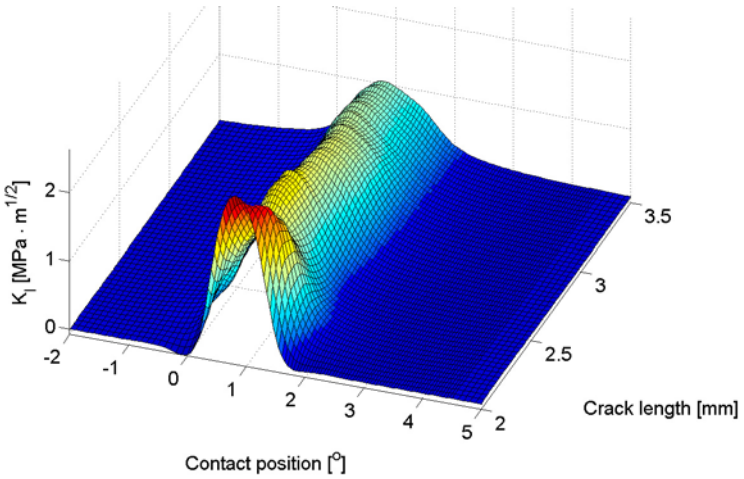

a) Without friction between crack faces

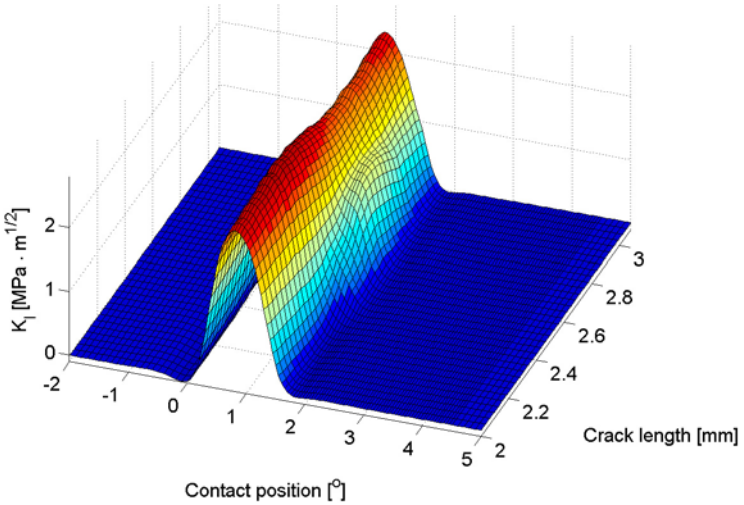

b) Friction coefficient $\mu = 0.1$

Fig. 17. K_I as a function of rolling contact position and crack depth

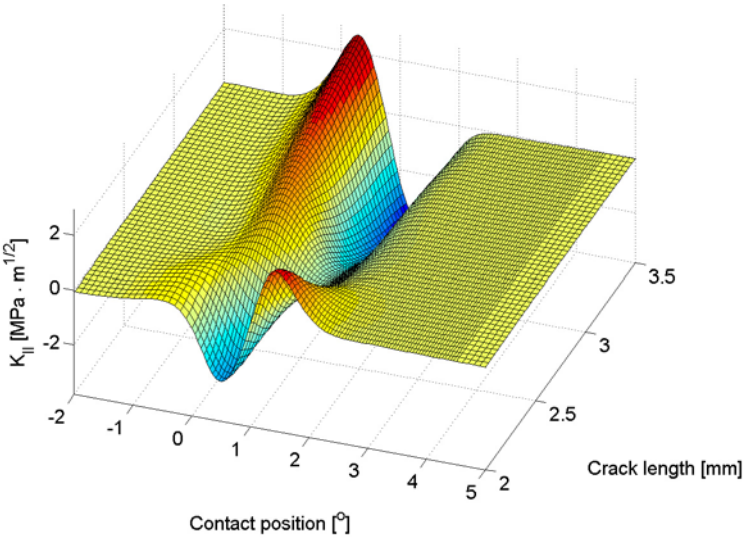

a) Without friction between crack faces

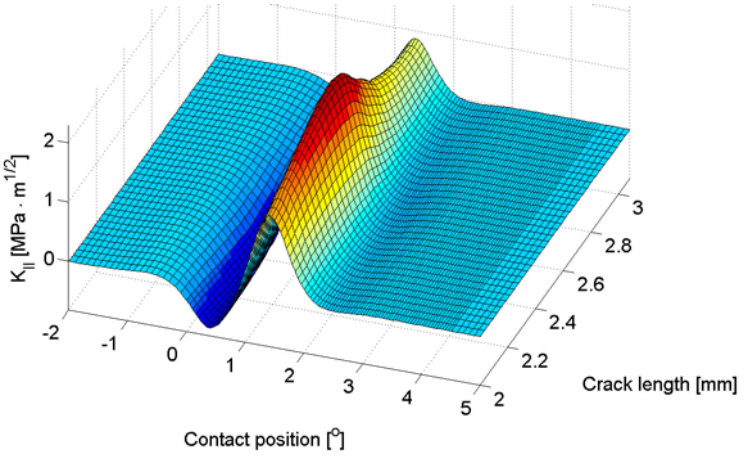

b) Friction coefficient $\mu = 0.1$

Fig. 18. K_{II} as a function of rolling contact position and crack depth

Specifically, for the initial crack without friction between crack faces $\Delta K_{II} \cong 9$ MPa m$^{1/2}$ but already with the friction coefficient $\mu = 0.1$ the mode II range ΔK_{II} decreases to 6 MPa m$^{1/2}$. Further, in the case when friction is not assumed between crack faces, the negative values of K_{II} prevail during the mode I cycle.

By contrast, the positive values of K_{II} during the mode I cycle are more dominant when the friction coefficient $\mu = 0.1$ is considered, see Fig. 15b. As a result, the maximum tensile stress range criterion predicts a positive value of crack deviation angle when friction is not assumed and crack propagates towards the wheel centre, see Fig. 16a. On the other side, a negative value of crack deviation angle is predicted in the latter case, and as a consequence, spalling may occur.

So far only normal contact forces in the wheel-rail contact were considered. However, the contact forces generally have also tangential part. According to the linear theory of rolling contact [21] the tangential force T exhibits a linear dependence on creepage, as it is also shown in Fig. 3. However, in reality it saturates at value $T = fN_c$, where $f = 0.2$ stands for the coefficient of friction between the wheel and rail, see e.g. [33] and N_c is the resulting normal contact force. Next, let us consider a saturated tangential force acting in the rolling contact. Two mutual configurations of crack and tangential contact force depicted in Fig. 19 are considered.

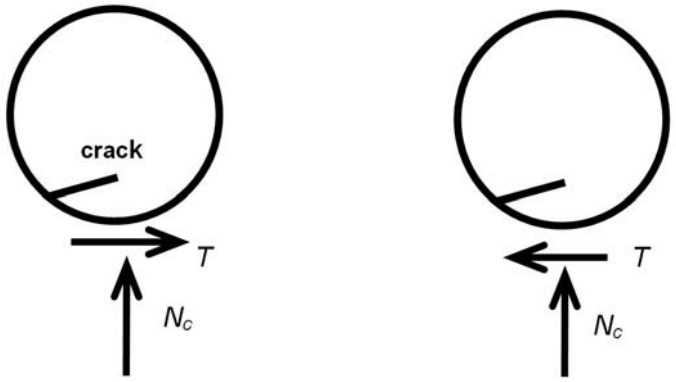

Fig. 19. Two mutual configurations of crack and tangential contact force

First, let us start with the configuration in Fig. 19a. Consider that the friction coefficient between crack faces $\mu = 0.1$. By inspection of Fig. 20 one can see that the loading of crack is very complex and it is not easy to examine the condition (2). Nevertheless, it is apparent that in the stage of rolling contact specified by the range of angles $\alpha \in (-1°; 1.4°)$ is K_I* always smaller than K_{II}, so the coplanar crack growth is possible if also the condition (1) is fulfilled. It is not true in the last stage of rolling contact specified by the range of angles $\alpha \in (-1.4°; 3°)$, where the condition (2) is not fulfilled. (Very similar result is obtained if the friction between crack faces is not considered.) It means that mode I controlled crack growth can be initiated during the latter stage. Fig. 21 shows predicted crack path in the solid railway wheel when the tangential part of contact force acts in the direction shown in Fig. 19a. The case when friction is not considered is shown in Fig. 21a while Fig. 21b pertains to the case when the coefficient of friction between crack faces $\mu = 0.1$ is prescribed. Crack path simulations indicate that crack follows a nearly radial path. Contrary to the calculations when the contact force is purely normal one, see Fig. 16, the presence of friction does not significantly influence the crack path.

Finally, the configuration shown in Fig. 19b is investigated. Consider that the friction coefficient between crack faces $\mu = 0.1$. By inspection of results in Fig. 23 one can see that contrary to the configuration shown in Fig. 19a the condition (2) is not fulfilled in the first stage of rolling contact, i.e. in the range of the contact position angle $\alpha \in (-2°, 1°)$. Note that a similar result is obtained if the friction between crack faces is included. It means that crack will deflect in this stage and the coplanar crack growth is not possible.

The predicted crack path in the solid railway wheel, when the tangential part of contact force acts in the direction shown in Fig. 19b, is displayed in Fig. 22. Apparently, crack path simulations show that spalling is preferred mode of fracture regardless of the presence of friction between crack faces.

Apparently, all presented results depend on the calculated variations of the stress intensity factors during rolling contact loading. It would be desirable to compare the calculated SIFs towards the results in literature. The authors carried out very careful check of available literature, however for specified boundary conditions no results for crack in rail wheels were found. However, there are many results for cracks in rails. Perhaps closest to the results from the point of view of boundary conditions are the results presented in Xiangyuan Xu et al. [35] in their Fig. 5, where boundary conditions including the friction coefficients are very close to the conditions used for the obtaining of results shown in Fig. 23a and Fig. 23b. Though the variations of SIFs differ significantly, their maximum values differ by 5 % in case of the results in Fig. 23 and by 33 % in case of the results in Fig. 23.

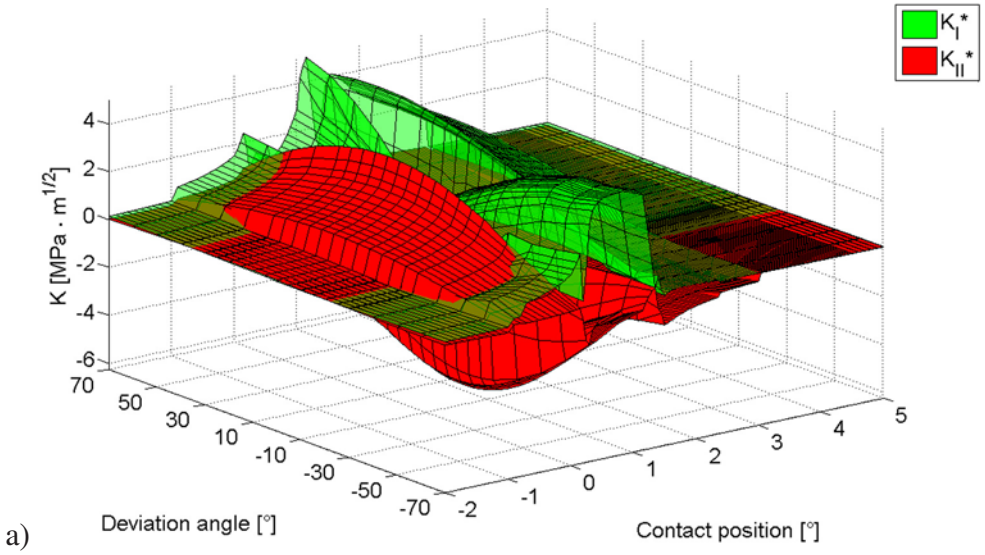

a)

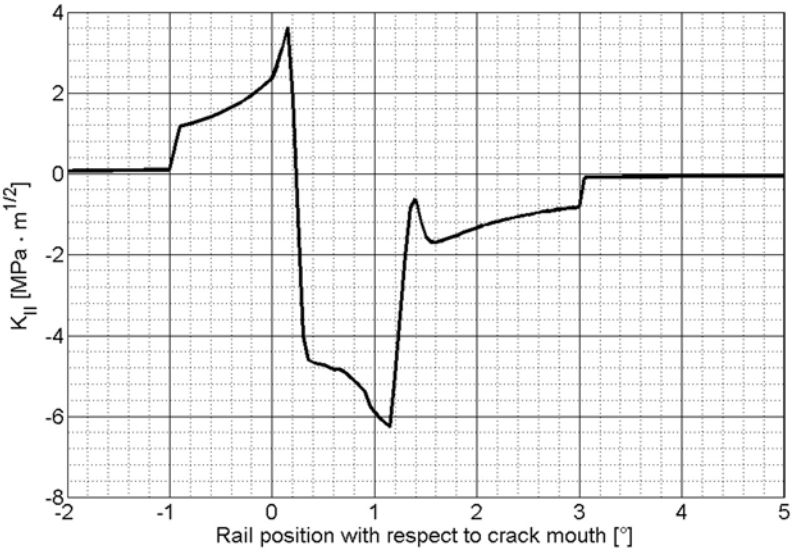

b)

Fig. 20. a) ΔK_I^* and ΔK_{II}^* on the short supplementary crack for a wide range of crack deviation angles as functions of rolling contact position with respect to crack mouth; b) ΔK_{II} on the starter crack as a function of rolling contact position with respect to crack mouth. Tangential contact force is considered according to the scheme in Fig. 19a. The friction coefficient between crack faces $\mu = 0.1$

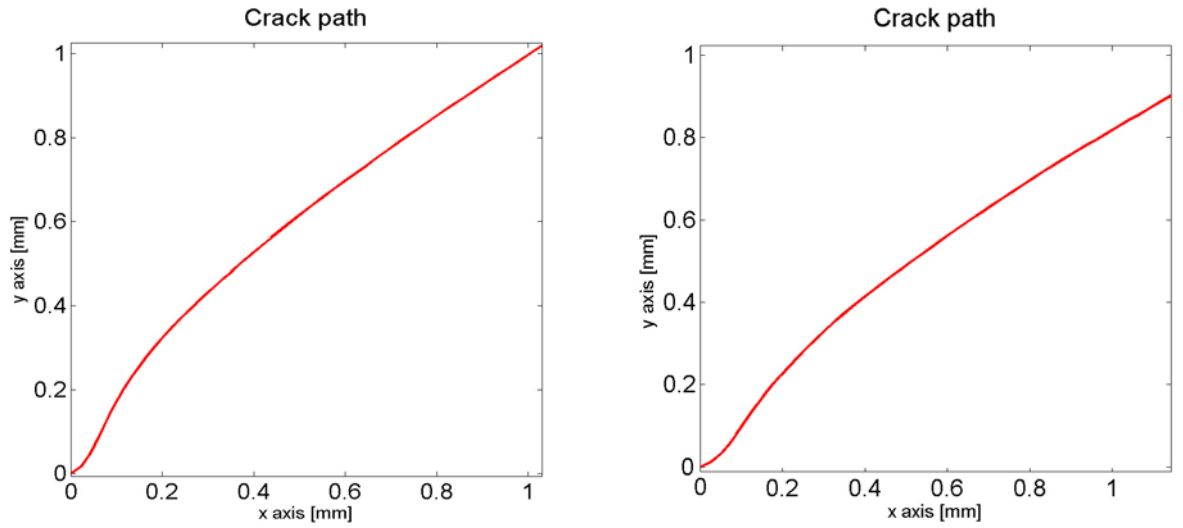

a) Without friction between crack faces b) Friction coefficient $\mu = 0.1$

Fig. 21. Predicted crack path in solid railway wheel. The tangential part of contact force acts in the direction shown in Fig. 19a

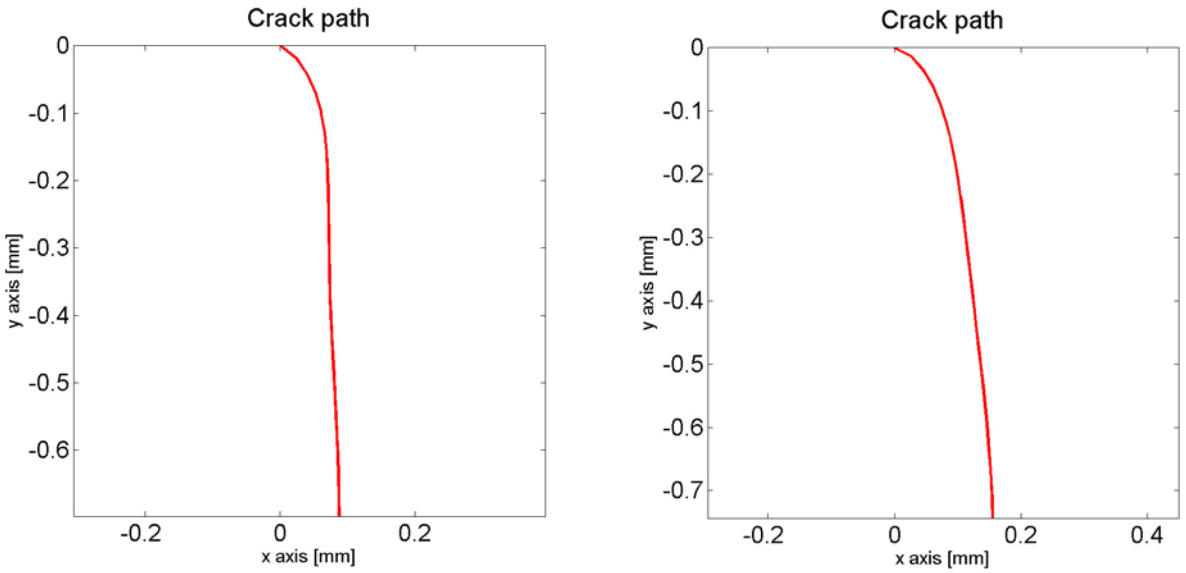

a) Without friction between crack faces b) Friction coefficient $\mu = 0.1$

Fig. 22. Predicted crack path in solid railway wheel. The tangential part of contact force acts in the direction shown in Fig. 19b

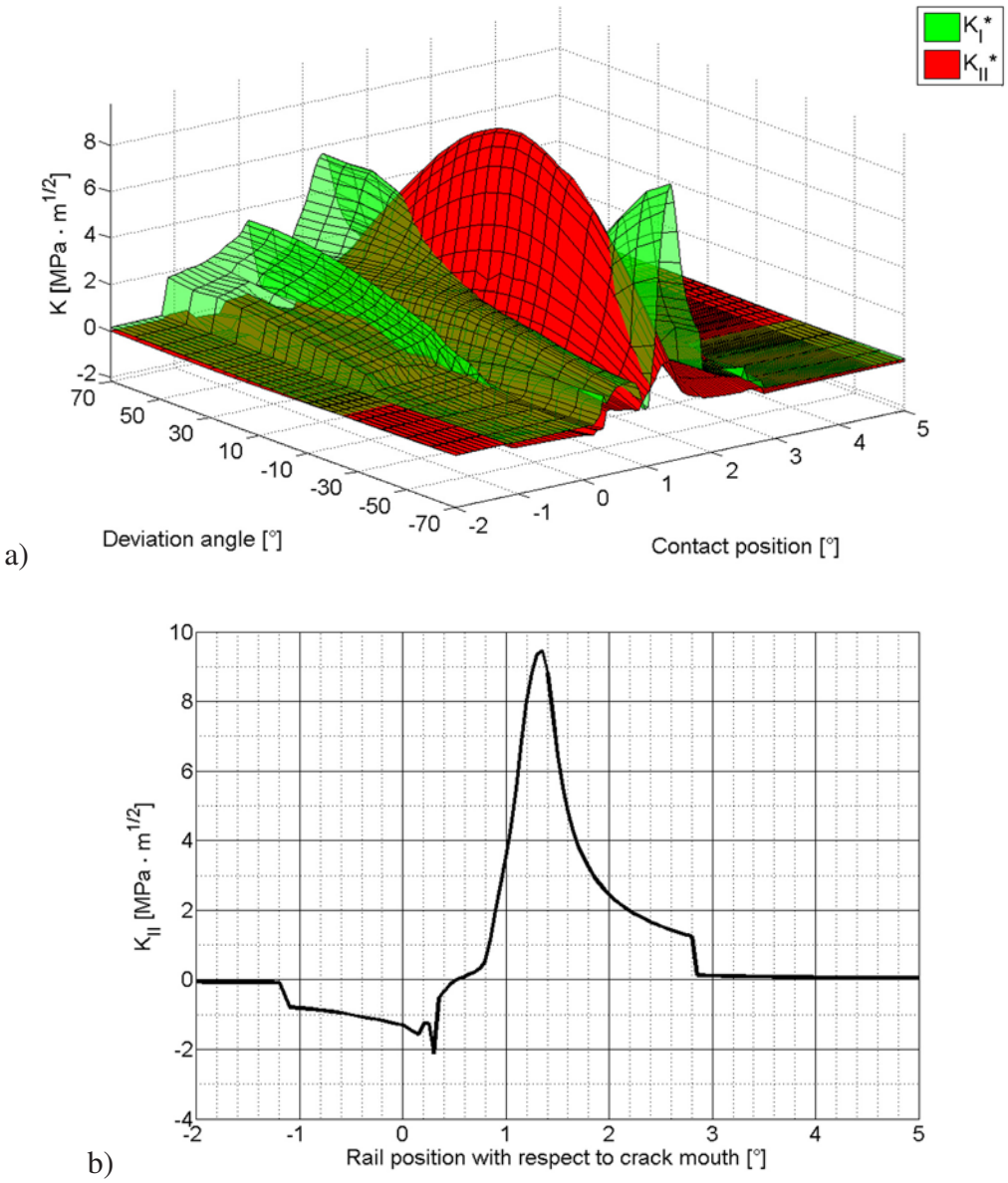

Fig. 23. a) ΔK_I* and $\Delta K_{II}*$ on the short supplementary crack for a wide range of crack deviation angles as functions of rolling contact position with respect to crack mouth; b) ΔK_{II} on the starter crack as a function of rolling contact position with respect to crack mouth. Tangential contact force is considered according to the scheme in Fig. 19b. The friction coefficient between crack faces $\mu = 0.1$

4. Concluding remarks

A computational 2D analysis of crack path for crack in a railway wheel rim was performed. Two basic configurations were considered: a crack on wheel rim fixed by an interference fit and a crack in a solid railway wheel. Plank and Kuhn criterion was used to decide whether crack would either kink and follow mode I controlled (tensile mode) path, or it will propagate coplanar mode II controlled (shear mode). If mode II controlled crack growth is not likely to be initiated, the crack deviates tensile mode controlled path. In the latter case the procedure of fatigue crack path prediction under non proportional loading was based on the assumption that the crack propagates in the direction perpendicular to the direction of the maximum tensile stress range $\Delta\sigma_{n,max}$.

The computational analysis based upon the linear fracture and contact mechanics approach allows drawing the following conclusions:

Crack path simulations in the RW rim show that the interference between the rim and the wheel influences significantly the crack path. Radial crack extension is preferred mode of fracture and the fatigue crack accelerates significantly with increasing crack depth. The friction between crack faces seems to support shear dominated fatigue crack growth, nevertheless the crack path does not change notably with friction. Hence, it may be stated that RW rim always failures in radial direction and coplanar crack growth is not probable.

Crack path simulations in solid railway wheel show that, under assumption of pure normal contact forces in the wheel-rail contact, spalling is preferred mode of fracture if the friction of crack faces is considered while a radial path occurs if the friction is zero. Nevertheless, in both cases coplanar crack growth is also possible mode of fracture. If also tangential part of contact force is taken into account, then it is shown that orientation of the tangential part of contact force matters. Specifically, the orientation illustrated in Fig. 19a promotes a radial crack path regardless of presence of the friction between crack faces. A coplanar crack growth may occur but mode I controlled crack growth is more probable. On the contrary, the orientation of the tangential part of contact force illustrated in Fig. 19b promotes spalling regardless of presence of the friction between crack faces and the coplanar crack growth does not occur.

Acknowledgements

The work has been supported by the NETME Centre established thanks to a financial support of the European Regional Development Fund under the Operational Program Research and Development for Innovation. The presented results have been obtained within NETME CENTRE PLUS (LO1202) project co-funded by the Czech Ministry of Education, Youth and Sports within the support program National Sustainability Program I.

Reference

[1] Andersson, C., Johansson, A., Prediction of rail corrugation generated by three-dimensional wheel — rail interaction, Wear 257 (2004) 423–434.

[2] Bogdański, S., Brown, M. W., Modelling the three-dimensional behaviour of shallow rolling contact fatigue cracks in rails, Wear 253 (2002) 17–25.

[3] Bogdański, S., Lewicki, P., 3D model of liquid entrapment mechanism for rolling contact fatigue cracks in rails, Wear 265 (2008) 1 356–1 362.

[4] Bogdański, S., Olzak, M., Stupnicki, J., Numerical modelling of a 3D rail RCF 'squat'-type crack under operating load, Fatigue & Fracture of Engineering Materials & Structures 21 (1998) 923–935.

[5] Bogdański, S., Olzak, M., Stupnicki, J., Numerical stress analysis of rail rolling contact fatigue cracks, Wear 191 (1996) 14–24.

[6] Bold, P. E., Brown, M. W., Allen, R. J., Shear mode crack growth and rolling contact fatigue, Wear 144 (1991) 307–317.

[7] Bower, A. F., The influence of crack face friction and trapped fluid on surface initiated rolling contact fatigue cracks, Journal of Tribology 110 (1988) 704–711.

[8] Dahlin, P., Olsson, M., The effect of plasticity on incipient mixed-mode fatigue crack growth, Fatigue & Fracture of Engineering Materials & Structures 26 (2003) 577–588.

[9] Doquet, V., Pommier, S., Fatigue crack growth under non-proportional mixed-mode loading in ferritic-pearlitic steel, Fatigue & Fracture of Engineering Materials & Structures 27 (2004) 1 051–1 060.

[10] Ekberg, A., Kabo, E., Fatigue of railway wheels and rails under rolling contact and thermal loading — an overview, Wear 258 (2005) 1 288–1 300.

[11] Ekberg, A., Kabo, E., Nielsen, J. C. O., Lundén, R., Subsurface initiated rolling contact fatigue of railway wheels as generated by rail corrugation, International Journal of Solids and Structures 44 (2007) 7 975–7 987.

[12] Ekberg, A., Sotkovszki, P., Anisotropy and rolling contact fatigue of railway wheels, International Journal of Fatigue 23 (2001) 29–43.

[13] Fletcher, D. I., Smith, L., Kapoor, A., Rail rolling contact fatigue dependence on friction, predicted using fracture mechanics with a three-dimensional boundary element model, Engineering Fracture Mechanics 76 (2009) 2 612–2 625.

[14] Guagliano, M., Sangirardi, M., Vergani, L., Experimental analysis of surface cracks in rails under rolling contact loading, Wear 265 (2008) 1 380–1 386.

[15] Hoffmeyer, J., Döring, R., Seeger, T., Vormwald, M., Deformation behaviour, short crack growth and fatigue livesunder multiaxial nonproportional loading, International Journal of Fatigue 28 (2006) 508–520.

[16] Hourlier, F., Pineau, A., Propagation of fatigue cracks under polymodal loading, Fatigue & Fracture of Engineering Materials & Structures 5 (1982) 287–302.

[17] Jacobson, B., Kalker, J. J., Rolling contact phenomena, Springer-Verlag Wien GmbH, New York, 2000.

[18] Jandora, R., Modelling of the railway wheelset movement considering real geometry, Engineering Mechanics 1 (2007) 105–106.

[19] Jandora, R., Numerical simulations of dynamic loads in wheel-rail contact with shape irregularities, Doctoral Thesis, Brno Univesity of Technology, 2012.

[20] Kabo, E., Ekberg, A., Fatigue initiation in railway wheels — a numerical study of the influence of defects, Wear 253 (2002) 26–34.

[21] Kalker, J. J., Paper I (iii) Elastic and viscoelastic analysis of two multiply layered cylinders rolling over each other with coulomb friction, Tribology Series 17 (1990) 27–34.

[22] Kalker, J. J., Three-dimensional elastic bodies in rolling contact, Springer – Science + Business Media, B.V., Waterloo, 1990.

[23] Kaneta, M., Murakami, Y., Propagation of semi-elliptical surface cracks in lubricated rolling/sliding elliptical contacts, Journal of Tribology 113 (1991) 270–275.

[24] Kaneta, M., Murakami, Y., Suetsugu, M., Mechanism of surface crack growth in lubricated rolling/sliding spherical contact, Journal of Applied Mechanics 53 (1986) 354–360.

[25] Kaneta, M., Yatsuzuka, H., Murakami, Y., Mechanism of crack growth in lubricated rolling/sliding contact, A S L E Transactions 28 (1985) 407–414.

[26] Plank, R., Kuhn, G., Fatigue crack propagation under non-proportional mixed mode loading, Engineering Fracture Mechanics 62 (1999) 203–229.

[27] Richard, H. A., Fulland, M., Sander, M., Theoretical crack path prediction, Fatigue & Fracture of Engineering Materials & Structures 28 (2005) 3–12.

[28] Richard, H. A, Sander, M., Fulland, M., Kullmer, G., Development of fatigue crack growth in real structures, Engineering Fracture Mechanics 75 (2008) 331–340.

[29] Ringsberg, J. W, Bergkvist, A., On propagation of short rolling contact fatigue cracks, Fatigue & Fracture of Engineering Materials & Structures 26 (2003) 969–983.

[30] Smith, R. A., Fatigue in transport: problems, solutions and future threats, Process Safety and Environmental Protection 76 (1998) 217–223.

[31] Taraf, M., Zahaf, E. H., Oussouaddi, O., Zeghloul, A., Numerical analysis for predicting the rolling contact fatigue crack initiation in a railway wheel steel, Tribology International 43 (2010) 585–593.

[32] Wallentin, M., Bjarnehed, H. L., Lundén, R., Cracks around railway wheel flats exposed to rolling contact loads and residual stresses, Wear 258 (2005) 1 319–1 329.

[33] Weber, R. L., Manning, K. V., White, M. W., College Physics, 4th Edition, USA, McGraw-Hill, 1965.

[34] Wong, S. L., Bold, P. E., Brown, M. W., Allen, R. J., A branch criterion for shallow angled rolling contact fatigue cracks in rails, Wear 191 (1996) 45–53.

[35] Xu, X., Cho, D.-H., Chang, Y.-S., Choi, J.-B., Kim, Y.-J, Jun, H.-K., Seo, J.-W., Kim, D.-S., Evaluation of slant crack propagation under RCF in railway rail, Journal of Mechanical Science and Technology 25 (2011) 1 215–1 220.

[36] Zerbst, U., Mädler, K., Hintze, H., Fracture mechanics in railway applications — an overview, Engineering Fracture Mechanics 72 (2005) 163–194.

[37] Zerres, P., Brüning, J., Vormwald, M., Fatigue crack growth behavior of fine-grained steel S460N under proportional and non-proportional loading, Engineering Fracture Mechanics 77 (2010) 1 822–1 834.